F. Topputo, D.A. Dei Tos, M. Rasotto, M. Nakamiya
The Sun–earth Saddle Point: Characterization and Opportunities to Test General Relativity
Celestial Mechanics and Dynamical Astronomy, Vol. 130, N. 4, 2018, 33 (20 pages)
doi:10.1007/s10569-018-9824-x

Celest Mech Dyn Astr manuscript No.
(will be inserted by the editor)

The Sun–Earth saddle point: Characterization and opportunities to test General Relativity

Francesco Topputo · Diogene A. Dei Tos · Mirco Rasotto · Masaki Nakamiya

Received: December 2017 / Accepted:

Abstract The saddle points are locations where the net gravitational accelerations balance. These regions are gathering more attention within the astrophysics community. Regions about the saddle points present clean, close-to-zero background acceleration environments where possible deviations from General Relativity can be tested and quantified. Their location suggests that flying through a saddle point can be accomplished by leveraging highly nonlinear orbits.

In this paper, the geometrical and dynamical properties of the Sun–Earth saddle point are characterized. A systematic approach is devised to find ballistic orbits that experience one or multiple passages through this point. A parametric analysis is performed to consider spacecraft initially on $L_{1,2}$ Lagrange point orbits. Sun–Earth saddle point ballistic fly-through trajectories are evaluated and classified for potential use. Results indicate an abundance of short-duration, regular solutions with a variety of characteristics.

Keywords Saddle point · Lagrange point · Ballistic orbits · General relativity

F. Topputo (✉) · D.A. Dei Tos
Department of Aerospace Science and Technology, Politecnico di Milano, Via La Masa 34, 20156 Milan, Italy
E-mail: francesco.topputo@polimi.it, diogenealessandro.deitos@polimi.it

M. Rasotto
Dinamica Srl, Piazza della Repubblica 10, 20121 Milan, Italy
E-mail: rasotto@dinamicatech.com

M. Nakamiya
Unit of Synergetic Studies for Space, Kyoto University, Kitashirakawa Oiwake-cho, Sakyo-ku, Kyoto 606-8502, Japan
E-mail: nakamiya.masaki.4c@kyoto-u.ac.jp

1 Introduction

Flying in highly nonlinear gravitational fields is becoming more and more appealing due to the unique features that can be achieved in these models: Lagrange point orbits (LPO) [12], ballistic captures [14], low-energy transfers [21], etc. These orbits generally require less Δv than the equivalent high-energy orbits. This reduction is enabled by a wise exploitation of the high sensitivity in initial conditions. Low-energy transfers have gained central importance in space mission analysis and design. These orbits provide improved mission versatility when compared to Keplerian solutions. In fact, they are used in astrodynamics to reduce fuel consumption [4], mitigate the risks associated to single-point burn failures [13], and accommodate wider launch windows [23].

Lately, attention has been paid to the exploration of the gravitational saddle points (SP) within the solar system [8,26,27]. These are locations where the net gravitational accelerations balance. Regions about the saddle points present clean, close-to-zero background acceleration environments where possible deviations from General Relativity (GR) can be tested and quantified. In particular, evidence is mounting that MOND (Modified Newtonian Dynamics) and TeVeS (Tensor-Vector-Scalar) theories can be valid for accelerations below 10^{-10} m/s^2 [16].

MOND is an alternative paradigm to Newtonian dynamics, originally formulated to explain anomalies in galaxies velocities without invoking non-baryonic dark matter. It constitutes a modification of dynamics in the limit of low accelerations that rests on the following basic assumptions [17]: i) There appears in physics a new constant, a_0, with the dimensions of acceleration; ii) Taking the formal limit $a_0 \to 0$ in all the equations of physics restores the equations of classical (pre-MOND) dynamics; and iii) For purely gravitational systems, the opposite, deep-MOND limit, $a_0 \to \infty$, gives limiting equations of motion that can be written in a form where the constants a_0 and G, and all masses in the problem, m_i, appear only in the product $m_i G a_0 = m_i/\mu_0$ where $\mu_0 = (G a_0)^{-1}$ [18]. Anomalous MOND/TeVeS gravity gradients $\geq 10^{-13}$m/s^2 are predicted within an elliptic bubble around saddle points [28]. Direct tests of the background acceleration in this region would provide unique information. An experiment can be conducted by flying a highly sensitive gradiometer through the SP region. Data points can either reveal deviations from GR or rule out once for all these speculations.

Among the saddle points in the solar system, the Sun–Earth one seems particularly appealing due to its relatively easy accessibility [3]: it is located at a distance of approximately 258,800 km from the Earth, along the Sun–Earth line, between the Sun and the Earth [5]. Its location and the nonequilibrium nature suggest that flying to the Sun–Earth SP can be accomplished by using highly nonlinear, underactuated orbits as opportunistic mission extension of spacecraft already about the Sun–Earth Lagrange points.

In this work, the geometrical and dynamical properties of the Sun–Earth SP are characterized in several dynamical models of increasing complexity. A systematic approach is then devised to find orbits that experience one or multiple passages through the saddle point in a ballistic way. A parametric analysis is performed to consider spacecraft initially on a number of LPO at different energies. Orbits are

sought in the Circular Restricted Three-Body Problem (CRTBP) with Sun and Earth as primaries, in the bicircular Restricted Four-Body Problem (RFBP) that includes the Moon, as well as in a full-ephemeris, three-dimensional restricted n-body model stated in a roto-pulsating frame incorporating non-gravitational forces [7], termed Roto-Pulsating Restricted n-Body Problem (RPRnBP). This design strategy follows the hierarchy of astrodynamical models presented in [6]. A large scale survey is completed encompassing more than $200,000$ initial conditions on several $L_{1,2}$ libration point orbits. Sun–Earth saddle point ballistic fly-through trajectories are evaluated and classified for potential use. Results indicate an abundance of short-duration, regular solutions with a variety of characteristics.

The remainder of this paper is organized as follows. After a brief description of the dynamical models in Section 2, the Sun–Earth saddle point geometry is analyzed in the CRTBP, RFBP, and RPRnBP (see Section 3). A dynamical characterization of the SP is then presented in Section 4, where trajectories that fly through the saddle point in a natural way for one or multiple times are sought. Critical remarks and recommendations are drawn in Section 5.

2 Dynamical models

2.1 The circular restricted three-body problem

Let us consider a body P of mass m in the vector field of two primaries P_1, P_2 of masses m_1 and m_2, respectively, such that $m \ll m_2 < m_1$. The primaries revolve in planar configuration at constant angular speed. The motion of P is studied in a rotating synodic reference frame, whose origin is located at P_1P_2 center of mass, the x axis is always aligned with the P_1P_2 direction, the z axis is orthogonal to their plane of motion, and the y axis forms a right-hand tern. By means of a proper scaling [20], the equations of motion depend only on $\mu = m_2/(m_1 + m_2)$. The scaling is such that the distance between the primaries, their angular speed, and the sum of their masses are set to a unity value. The positions of P_1 and P_2 are thus fixed, P_1 being located at $(-\mu, 0, 0)$, and P_2 at $(1-\mu, 0, 0)$. The equations of motion read

$$\boldsymbol{x}' = \boldsymbol{f}_3(\boldsymbol{x}) := \left(u, v, w, 2v + \Omega_{/x}, -2u + \Omega_{/y}, \Omega_{/z}\right)^{\mathrm{T}}, \tag{1}$$

where $\boldsymbol{x} := (x, y, z, u, v, w)^{\mathrm{T}}$ is P state, primes denote derivatives w.r.t. nondimensional time, and slashed subscripts are partial derivatives. The three-body pseudo-potential is

$$\Omega = \frac{1}{2}(x^2 + y^2) + \frac{1-\mu}{r_1} + \frac{\mu}{r_2} + \frac{1}{2}\mu(1-\mu), \tag{2}$$

where $r_1 = ((x+\mu)^2+y^2+z^2)^{1/2}$, $r_2 = ((x-1+\mu)^2+y^2+z^2)^{1/2}$ are the distances between P and P_1, P_2, respectively.

2.2 The bicircular restricted four-body problem

Let us now consider a perturber P_3 of mass m_3 such that $m \ll m_3 < m_2 < m_1$. P_1, P_2, and P_3 move in planar configuration at constant angular speed such that P_1 and P_2 revolve in circular orbits around their barycenter, while P_3 moves in circular orbit around P_2. The motion of P is studied in the reference frame introduced in the CRTBP. The following quantities are introduced: 1) $\mu_3 = m_3/(m_1+m_2)$, 2) P_2P_3 distance, a_3, and 3) P_3 angular velocity in inertial and synodic coordinates, n_3 and ω_3, respectively. All these quantities are not independent. The following relations hold (see [6] for more details):

$$\omega_3 = n_3 - 1, \qquad a_3^3 n_3^2 = \mu + \mu_3. \tag{3}$$

The equations of motion for P read

$$\boldsymbol{x}' = \boldsymbol{f}_4(\boldsymbol{x}) := \left(u, v, w, 2v + \Omega_{/x} + U_x, -2u + \Omega_{/y} + U_y, \Omega_{/z} + U_z\right)^{\mathrm{T}}, \tag{4}$$

where $\boldsymbol{U} = [U_x, U_y, U_z]^{\mathrm{T}}$ is the perturbing acceleration due to P_3,

$$\boldsymbol{U} = \mu_2 \left[(1-\mu) \frac{\boldsymbol{\rho}_1 - \boldsymbol{\rho}_3}{\|\boldsymbol{\rho}_1 - \boldsymbol{\rho}_3\|^3} + \mu \frac{\boldsymbol{\rho}_2 - \boldsymbol{\rho}_3}{\|\boldsymbol{\rho}_2 - \boldsymbol{\rho}_3\|^3} - \frac{\boldsymbol{\rho} - \boldsymbol{\rho}_3}{\|\boldsymbol{\rho} - \boldsymbol{\rho}_3\|^3} \right], \tag{5}$$

and $\boldsymbol{\rho}_3$ is the position of P_3 in the rotating frame,

$$\boldsymbol{\rho}_3 = \boldsymbol{\rho}_2 + a_3 \left(\cos\alpha, \sin\alpha, 0\right)^{\mathrm{T}}, \tag{6}$$

with $\alpha = \omega_3 f$ is the phase angle of P_3 with respect to the P_1P_2 line, and f is the nondimensional time. The CRTBP and the RFBP presented so far are later used by assuming $P_1 = \text{Sun}$, $P_2 = \text{Earth}$, and $P_3 = \text{Moon}$.

2.3 Roto-pulsating restricted n-body problem

In the RPRnBP, the motion of P is subject to the gravitational attractions of $n-1$ primaries, P_i, $i = 1, \ldots, n-1$, which move under their mutual gravitational attractions, and whose motion is given. The primaries are assumed oblate, and the force exerted by the Solar Radiation Pressure (SRP) on P is considered as well. Let $\boldsymbol{R}$ and $\boldsymbol{V}$ be the dimensional position and velocity of P in a reference frame centered at solar system barycenter, and let $\boldsymbol{\rho}$ and $\boldsymbol{\eta}$ be the corresponding nondimensional quantities in a rotating and pulsating frame of reference defined by P_1 and P_2. The equations of the RPRnBP are written as perturbation of the CRTBP by means of time-dependent coordinates and time transformations [7, 10]:

$$\boldsymbol{R}(t) = \boldsymbol{b}(t) + k(t)C(t)\boldsymbol{\rho}(\tau), \tag{7a}$$

$$\boldsymbol{V}(t) = \dot{\boldsymbol{b}} + \dot{k}C\boldsymbol{\rho} + k\dot{C}\boldsymbol{\rho} + \dot{\tau}kC\boldsymbol{\rho}', \tag{7b}$$

$$\tau = \omega(t - t_0), \tag{7c}$$

where

$$\mathbf{b}(t) = \frac{m_1\mathbf{R}_1 + m_2\mathbf{R}_2}{m_1+m_2}, \quad k(t) = \|\boldsymbol{R}_2 - \boldsymbol{R}_1\|, \quad \mathcal{C}(t) = [\mathbf{e}_1, \mathbf{e}_2, \mathbf{e}_3]\,, \tag{8}$$

with

$$\mathbf{e}_1 = \frac{\boldsymbol{R}_2 - \boldsymbol{R}_1}{k}, \qquad \mathbf{e}_2 = \mathbf{e}_3 \times \mathbf{e}_1, \qquad \mathbf{e}_3 = \frac{(\boldsymbol{V}_2 - \boldsymbol{V}_1)\times(\boldsymbol{R}_2 - \boldsymbol{R}_1)}{\|(\boldsymbol{V}_2 - \boldsymbol{V}_1)\times(\boldsymbol{R}_2 - \boldsymbol{R}_1)\|}. \tag{9}$$

The coordinates transformation in Eq. (7a) is composed by (1) A translation of the origin from the solar system barycenter to P_1P_2 barycenter, $\mathbf{b}(t)$; (2) A nondimensionalization with the factor $k(t)$, that is the actual P_1P_2 distance; and (3) A rotation by means of the orthogonal cosine angle matrix, $\mathcal{C}(t)$. As a result, the new frame rotates and pulsates in a nonuniform fashion and the primaries are at rest on the x-axis. P_1 and P_2 positions are $\boldsymbol{\rho}_1 = [-\mu, 0, 0]^\top$ and $\boldsymbol{\rho}_2 = [1-\mu, 0, 0]^\top$, respectively. The time transformation, Eq. (7c), (1) Shifts the initial epoch to t_0, and (2) Scales the time unit by means of the primaries mean motion about their common barycenter, ω. By choosing a constant mean motion, the average primaries revolution period is 2π and $\dot{\tau} = \omega$.

The equations of motion for the roto-pulsating restricted n-body problem are derived by applying coordinates and time transformations of Eqs. (7) to the restricted and inertial form of the Newton's gravitational equations. These reads:

$$\begin{aligned}\boldsymbol{\eta}' + \frac{1}{\omega}\left(\frac{2\dot{k}}{k}I + 2C^{\mathrm{T}}\dot{C}\right)\boldsymbol{\eta} + \frac{1}{\omega^2}\left(\frac{\ddot{k}}{k}I + 2\frac{\dot{k}}{k}C^{\mathrm{T}}\dot{C} + C^{\mathrm{T}}\ddot{C}\right)\boldsymbol{\rho} + \\ + \frac{1}{\omega^2}\left(\frac{C^{\mathrm{T}}\ddot{\boldsymbol{b}}}{k} + \frac{\nabla V}{k^2}\right) = \frac{SP_0}{\omega^2 k^3}\frac{\boldsymbol{\rho} - \boldsymbol{\rho}_s}{\|\boldsymbol{\rho} - \boldsymbol{\rho}_s\|^3}.\end{aligned} \tag{10}$$

In Eq. (10), primes and dots denote derivatives with respect to nondimensional and dimensional time, respectively, I is the 3-by-3 identity matrix, and the RPRnBP pseudo-potential gradient is

$$\nabla V = \sum_{j\in\mathcal{S}} \hat{\mu}_j \left[\frac{\boldsymbol{\rho} - \boldsymbol{\rho}_j}{\|\boldsymbol{\rho} - \boldsymbol{\rho}_j\|^3} + J_{2_j} R_{B_j}^2 \left(\frac{3I + 2I_z}{\|\boldsymbol{\rho} - \boldsymbol{\rho}_j\|^5} - \frac{5I(\boldsymbol{\rho} - \boldsymbol{\rho}_j)^{\mathrm{T}} I_z (\boldsymbol{\rho} - \boldsymbol{\rho}_j)}{\|\boldsymbol{\rho} - \boldsymbol{\rho}_j\|^7}\right)(\boldsymbol{\rho} - \boldsymbol{\rho}_j)\right], \tag{11}$$

where $\mathcal{S}$ is the set of $n-1$ primaries included in the model, $\hat{\mu}_j = Gm_j$ is the gravitational parameter of the j-th celestial body, J_{2j} its second harmonic coefficient related to the inhomogeneous mass distribution, R_{B_j} its equatorial radius, I_z is a 3-by-3 null matrix except for the third diagonal component, which is one, and $\boldsymbol{\rho}_s$ is the Sun position vector. Moreover, SP_0 is the SRP parameter on P,

$$SP_0 = (1 + c_r)\frac{A}{m}\frac{\Psi_0 d_0^2}{c}, \tag{12}$$

where c_r is the reflectivity coefficient of P, A/m its area-to-mass ratio, Ψ_0 the solar flux intensity at a distance d_0 from the Sun, and c the speed of light in vacuum. Table 1 gives values of the parameters used in this work and SPICE[1] estimates for the mean Sun–Earth–Moon system parameters.

[1] SPICE is NASA's Observation Geometry and Information System for Space Science Missions [1,2]. `https://naif.jpl.nasa.gov/naif`; last downloaded on February 7, 2018.

Table 1: Parameters of the Sun–Earth–Moon system.

Parameter	Symbol	Value
Earth gravitational parameter	$\hat{\mu}_1$	398600.4354360959 km^3/s^2
Sun–Earth mass ratio	μ	$3.003480593992993 \times 10^{-6}$
Moon mass parameter	μ_3	$3.694292214919400 \times 10^{-8}$
Length unit	LU	$1.495978706136889 \times 10^6$ km
Time unit	TU	58.13235351684487 days
Velocity unit	VU	29.78473657194809 km/s
Earth mean radius	R_{B_2}	6371.008366666666 km
Moon mean radius	R_{B_3}	1737.4 km
Earth oblateness coefficient	J_{2_2}	0.001082616
Moon oblateness coefficient	J_{2_3}	0
SRP parameter	SP_0	$2.210656810849369 \times 10^6$ km^3/s^2
Earth–Moon distance	a_3	0.002569555291283
Moon synodic angular speed	ω_3	12.386902201906503
L_1 location w.r.t. Earth	x_{L_1}	$-1.491551005309341 \times 10^6$ km
L_2 location w.r.t. Earth	x_{L_2}	$1.501531764462003 \times 10^6$ km
Reflectivity coefficient	c_r	0.08
Area-to-mass ratio	A/m	0.02 m^2/kg

Equations (10) are integrated with double precision using a $7^{\text{th}}/8^{\text{th}}$ order variable step Runge–Kutta–Fehlberg scheme with absolute and relative error tolerances set to 2.5×10^{-14}. The integration is stopped in case a crash event is found, defined to occur when P distance with respect to the attractor is less or equal than its mean radius. The RPRnBP has been validated against GMAT[2]. Table 2 reports the difference between this work and GMAT when integrating the initial state of LISA Pathfinder for 100 days. In the following, parallel computations are performed with a hub of 80 Intel$^{\text{TM}}$ Xeon$^{\text{TM}}$ CPUs E5-4620 v4 at 2.1 GHz with 256 Gb of RAM[3].

Table 2: Validation errors of RPRnBP against GMAT.

Object	Position error [km]	Velocity error [mm/s]
Lisa PathFinder	1.080	106.020

[2]GMAT is NASA's General Mission Analysis Tool. `https://gmat.gsfc.nasa.gov/`; Last downloaded on March 9, 2017

[3]This is the Euler workstation at the Department of Aerospace Science and Technology, Politecnico di Milano.

3 A hierarchical characterization of the Sun–Earth saddle point

The Sun–Earth saddle point is analyzed in three models of increasing complexity:

1. Sun–Earth circular restricted three-body problem (CRTBP), where by definition the SP is fixed with respect to the synodic reference frame.
2. Bicircular restricted four-body problem (RFBP) having the Sun, the Earth, and the Moon as primaries, in which the SP follows a periodic oval trajectory.
3. High-fidelity roto-pulsating restricted n-body problem (RPRnBP), where the SP motion is dominated by the gravitational terms of the solar system.

By definition, the gravitational saddle point is the location in the configuration space where the net gravitational acceleration balances. In an inertial frame, the SP position is thus calculated by solving

$$\boldsymbol{F}(\boldsymbol{R}_{\mathrm{SP}}) := \sum_{j\in\mathcal{S}} \hat{\mu}_j \frac{\boldsymbol{R}_j - \boldsymbol{R}_{\mathrm{SP}}}{\|\boldsymbol{R}_j - \boldsymbol{R}_{\mathrm{SP}}\|^3} = \boldsymbol{0}, \tag{13}$$

for $\boldsymbol{R}_{\mathrm{SP}}$ once the positions of primaries, $\boldsymbol{R}_j$, are known.

3.1 Saddle point in the CRTBP

The application of the CRTBP transformation to Eq. (13) yields

$$\boldsymbol{F}_3(\boldsymbol{\rho}_{\mathrm{SP}}) := (1-\mu)\frac{\boldsymbol{\rho}_{\mathrm{SP}} - \boldsymbol{\rho}_1}{\|\boldsymbol{\rho}_{\mathrm{SP}} - \boldsymbol{\rho}_1\|^3} + \mu\frac{\boldsymbol{\rho}_{\mathrm{SP}} - \boldsymbol{\rho}_2}{\|\boldsymbol{\rho}_{\mathrm{SP}} - \boldsymbol{\rho}_2\|^3} = \boldsymbol{0}. \tag{14}$$

Eq. (14) possesses an analytic solution. Let $\boldsymbol{\rho}_{\mathrm{SP}} = [x_{\mathrm{SP}}, y_{\mathrm{SP}}, z_{\mathrm{SP}}]^\top$, then

$$x_{\mathrm{SP}} = 1 - \frac{\sqrt{\mu - \mu^2} - 2\mu^2}{1-2\mu}, \qquad y_{\mathrm{SP}} = 0, \qquad z_{\mathrm{SP}} = 0. \tag{15}$$

The Sun–Earth SP is $258,813.23$ km away from the Earth in the Sun direction.

3.2 Saddle point in the RFBP

In the bicircular restricted four-body problem, the saddle point location is influenced by the presence of an additional celestial body (P_3). The application of the RFBP transformation to Eq. (13) yields

$$\boldsymbol{F}_4(\boldsymbol{\rho}_{\mathrm{SP}}) := (1-\mu)\frac{\boldsymbol{\rho}_{\mathrm{SP}} - \boldsymbol{\rho}_1}{\|\boldsymbol{\rho}_{\mathrm{SP}} - \boldsymbol{\rho}_1\|^3} + \mu\frac{\boldsymbol{\rho}_{\mathrm{SP}} - \boldsymbol{\rho}_2}{\|\boldsymbol{\rho}_{\mathrm{SP}} - \boldsymbol{\rho}_2\|^3} + \mu_3\frac{\boldsymbol{\rho}_{\mathrm{SP}} - \boldsymbol{\rho}_3}{\|\boldsymbol{\rho}_{\mathrm{SP}} - \boldsymbol{\rho}_3\|^3} = \boldsymbol{0}. \tag{16}$$

Eq. (16) has no closed-form solution. In the Sun–Earth–Moon case, it can be parameterized for the Moon phase angle α and solved numerically over a lunar period. Eq. (16) is solved numerically with Levenberg-Marquardt root-finding method [15], with a tolerance of 10^{-24}. The CRTBP fixed location is used as initial guess to

start the solver. The SP trajectory is then interpolated by means of a piecewise cubic spline for efficient access. As expected, the saddle point in the RFBP lies on the xy plane ($z_{\mathrm{SP}} = 0$).

Figure 1 shows the SP trajectory on the xy plane in the RFBP (thick solid line). In the left of Figure 2, the RFBP saddle point trajectory is displayed in the neighborhood of its CRTBP counterpart, and in the right of Figure 2 the saddle point x and y trends are shown as function of the Moon phase. The saddle point trajectory is symmetric with respect to the x axis because so is the Moon motion. The saddle point Moon-triggered location shift is more pronounced in the right portion of its trajectory, reaching approximately 6000 km at its farthest point from the CRTBP SP. In this configuration, $\alpha = \pi$, that is, the Moon lies between the Sun and Earth and is aligned to them. In the opposite configuration ($\alpha = 0$), when the Moon lies after the Earth on the x axis, the effect on the SP trajectory is comparatively less intense. As a result, a bubble-like path emerges about the left side of the CRTBP SP that can be appreciated in the magnification on the left of Figure 2. Also, the SP moves slower when it is closer to its CRTB counterpart, which also means that the RFBP SP sticks closer to its CRTBP approximation for most of its trajectory (this is also true in the RPRnBP). This phenomenon motivates the use of a fix SP location in preliminary trajectory design phases. Table 3 shows the duration in percentile of lunar periods for which RFBP SP is closer than a certain distance threshold, d, to its CRTBP approximation.

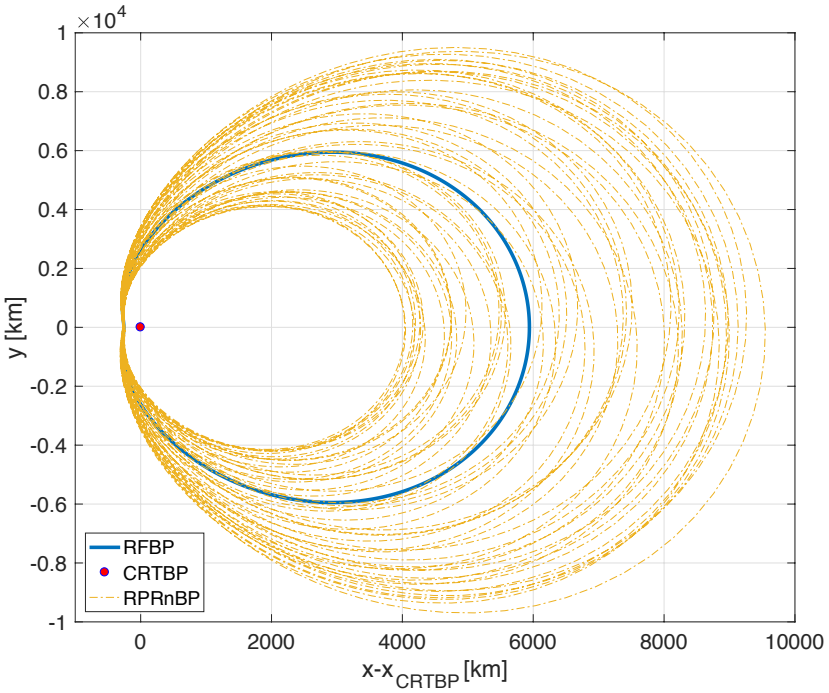

Fig. 1: Saddle point trajectory in the RFBP (thick solid line) and in the restricted n-body problem (thin dashed line). The reference is the Sun–Earth synodic frame.

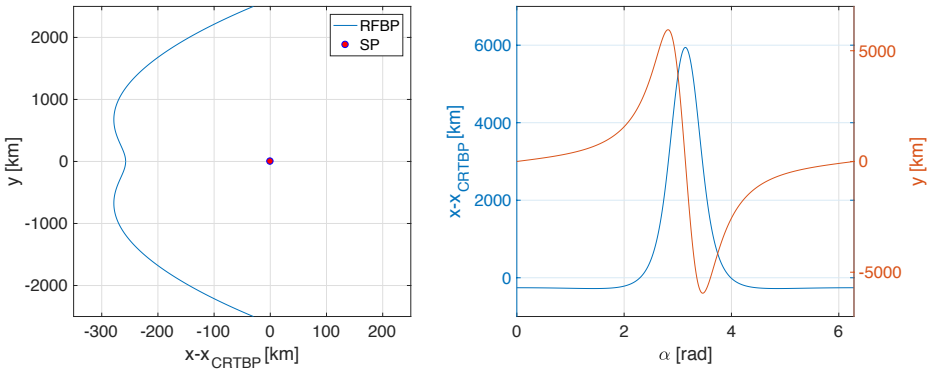

Fig. 2: RFBP SP trajectory in the vicinity of its CRTBP location (left) and RFBP SP trajectory as function of the Moon phase angle over one lunar revolution (right).

Table 3: Percentile duration for discrete saddle point shift thresholds.

Parameter	Units	Values					
d	10^3 km	1	2	3	4	5	6
Duration	%	53.44	68.24	75.40	80.04	83.68	88.24

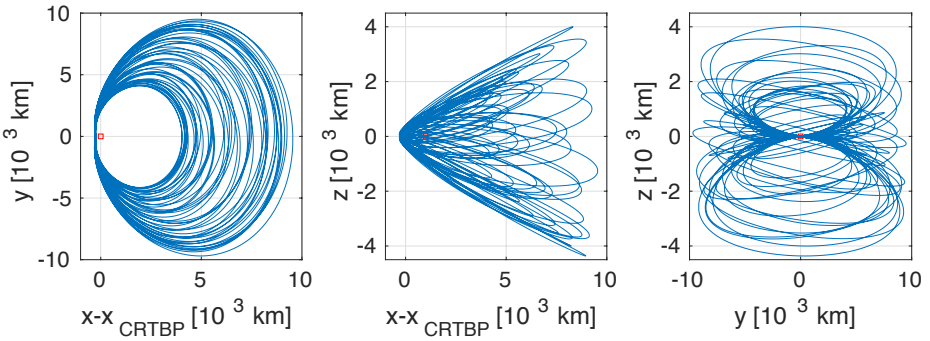

Fig. 3: Saddle point trajectory in a Sun–Earth synodic frame in the RPRnBP. From left to right, the projection onto the xy, xz, and yz planes.

3.3 Saddle point in the RPRnBP

Eq. (13) is applied to the set of major celestial bodies in the solar system, namely, the Sun, the Earth, the Moon, the barycenter of the remaining 7 planetary systems, and Pluto. The solution is found numerically. To ease the converge at each time step, an initial guess equal to the CRTBP SP is again provided.

The dashed line in Figure 1 represents the SP trajectory projected on the xy plane, whereas Figure 3 displays the full projections. The SP trajectory in the RPRnBP

differs from its RFBP path by a maximum distance of 3600 km in the synodic plane, and of 4000 km out of plane.

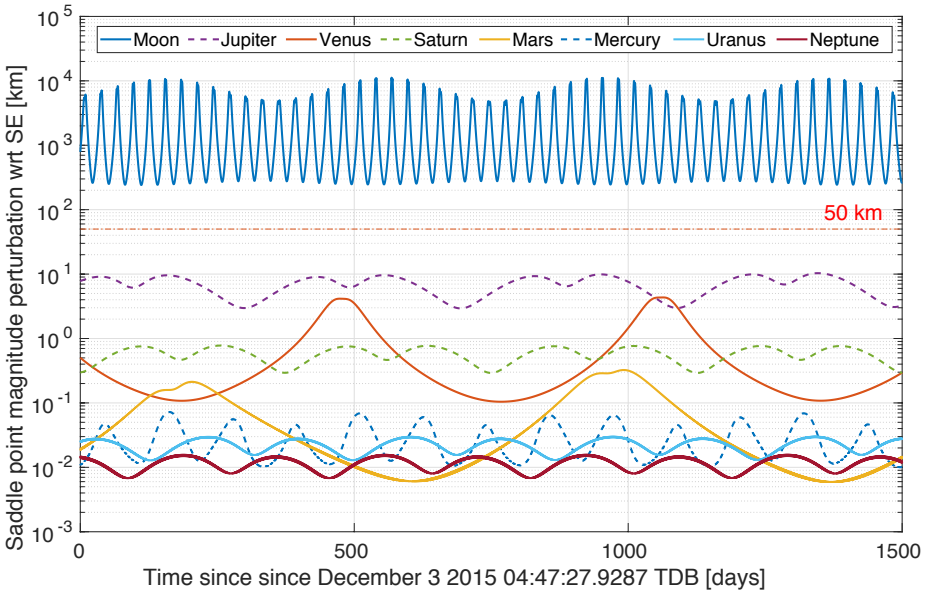

Fig. 4: Difference of the perturbed saddle point location (single celestial body active per line) and its nominal CRTBP location (semi-logarithmic scale). The perturbations are computed for 1500 days.

Figure 4 shows, for each celestial body considered, the saddle point shift with respect to its CRTBP position in a semi-logarithmic scale. The lunar gravity causes the largest perturbation, ranging from 240 km to 11,200 km. Jupiter and Venus on the other hand shift the SP location of maximum 10 km and 4 km, respectively. A mission that has to hit the saddle region with a precision of, say, 50 km must thus account for these perturbative actions, in particular the Moon, Jupiter, and Venus [24,25]. The gravitational field generated by the Milky Way also plays a role in determining the exact position of the SP. The SP shift corresponding to the galaxy gravity is estimated at 10 m in [27], assuming a uniform galaxy background gravitation across the solar system, and at few centimeters in [9], assuming that the Sun orbit around the center of the Galaxy is in centrifugal equilibrium. The Milky Way contribution is therefore neglected in this work.

4 Saddle point ballistic fly-through opportunities

A thorough exploration of the solution space, by means of a grid search, aims at extracting preliminary information on the cost, time, and, more generally, bounds of the design variables. The goal is to explore the search space to detect orbits

performing one (or multiple) SP passage(s) in a ballistic fashion. The focus is on LPO missions, deemed good candidates for opportunistic mission extensions. In this analysis, departure conditions are set within the regions about the Sun–Earth $L_{1,2}$. The output of this analysis may be used as a feasible initial guess for an optimization for the problem of accurate SP targeting.

The exploration of the solution space for orbits leaving the Sun–Earth LPO regions and flying through the SP is implemented in three steps:

1. *Search space sampling in the CRTBP.* This is done to analyze the relative geometry and the phasing conditions between LPO invariant manifolds and the fix SP location. By neglecting the influence of the Moon, preliminary results are gathered on the LPOs-to-SP trajectories existence, geometry, and cost.
2. *Search space sampling in the Sun–Earth–Moon RFBP.* In this analysis the gravitational pull of the Moon, albeit on a simplified level, acts as a chaos-inducer for the motion of P. This significantly increases the diversity and abundance of solutions ballistically flying close to the saddle point. The role of the Moon in modifying the solutions of interest is analyzed in detail.
3. *Search space sampling in the RPRnBP.* The solution space exploration is performed directly within the high-fidelity RPRnBP. Accordingly, this analysis gives the most realistic results for ballistic transfers from the Sun–Earth LPO region to the saddle point.

4.1 Methodology

Regardless the dynamical model, the exploration of the solutions space is performed with a specific set of initial conditions. It is assumed that the spacecraft (S/C) initially lies on a halo orbit about either L_1 or L_2, defined in the CRTBP. The spacecraft is then injected into a branch of the unstable manifold associated to the halo, and it is free to move in the Sun–Earth–Moon region. The displacement along the unstable direction is on average 150 km in position and 3 cm/s in velocity. Accordingly, initial position and velocity are specified with:

(i) The halo out-of-plane amplitude, A_z. In the following, only the southern family is considered. Different values of A_z uniquely correspond to different Jacobi energies. Hence, given any of these two parameters, one particular halo orbit is specified [11].

(ii) The nondimensional time along the periodic halo orbit, t_{po}. This parameter univocally specifies the S/C state along a halo [22].

(iii) A phasing parameter, which specifies either an angular lunar phasing in the RFBP, or a true date for the RPRnBP case. The parameter allows to uniquely determine the states of all retained celestial bodies. This is not needed within the CRTBP, due to its autonomous nature.

Fine searching is then performed on these three parameters, which specify a set of initial conditions. Each initial condition is flown within the correct dynamical model for a fixed duration, or time of flight (TOF). Here, TOF is set to 3 years.

Eventually, solutions are ranked according to their geometry. In particular, trajectories crossing a 10,000 km circular bubble around the SP (either fixed or moving) are considered and labeled. In this work, all trajectories flying through the bubble encircling the SP are interchangeably termed passage or fly-through. The distance of 10,000 km from the SP is deemed to be sufficiently small to be regarded as close passage at the Sun–Earth scales. On top of that, this distance can be zeroed by means of a successive optimization step [25]. This strategy is undertaken because it 1) Reduces the dimension of the search space by initially locating the S/C on the halo unstable manifold; 2) Maximizes the chances of the S/C to permanently leave the LPOs region along an unstable direction; and 3) Prevents solutions from being restricted by a SP accurate fly-through.

4.2 Exploration in the Sun–Earth CRTBP

The spacecraft lies initially in a halo orbit about either $L_{1,2}$ and is then injected into a branch of its unstable manifold. The bounds and resolution of the fine search are defined in Table 4. The analysis in the CRTBP ultimately provides insights on the halo unstable manifolds relative geometry with the SP. The example of $A_z = 10^5$ km is shown in Figure 5. In this case, $t_{\mathrm{po}} = 0$ corresponds to the leftmost state of the orbit as seen in the xy plane; t_{po} increases by flowing in the clockwise direction until $t_{\mathrm{po}} = T_{\mathrm{po}}$, that is the period of the periodic orbit.

In this search space, 119 and 36 transfers (1.65% and 0.5% of the search space) from L_1 and L_2, respectively, fly closer to the SP than the threshold of 10,000 km. A few important remarks stem from this analysis: (a) No ballistic multiple SP passage is obtained in the CRTBP with the current search settings (7,200 samples); and (b) The unstable manifolds tube does not fully encircle the saddle point, setting a limit to the opportunities for ballistic SP fly-through.

4.3 Exploration in the Sun–Earth–Moon RFBP

States on the halo unstable manifolds, defined in the CRTBP, are now propagated within the RFBP. In addition, the lunar phase angle is included in the search space. A total of 86,400 transfers (10 A_z samples $\times$ 720 t_{po} samples $\times$ 12 Moon phase samples) are computed to investigate the geometric relation between the manifold and the saddle point. Table 5 shows the bounds of the fine search for the exploration in the RFBP. The SP is assumed to be fixed at its CRTBP location. This assumption is justified, given the limited duration the actual SP travels far

Table 4: Bounds of the search space in the CRTBP.

Symbol	Description	Units	Range	Step
A_z	Size of the halo orbit	km	50,000 - 500,000	50,000
t_{po}	Time along the halo	–	0 - T_{po}	$T_{\mathrm{po}}/720$

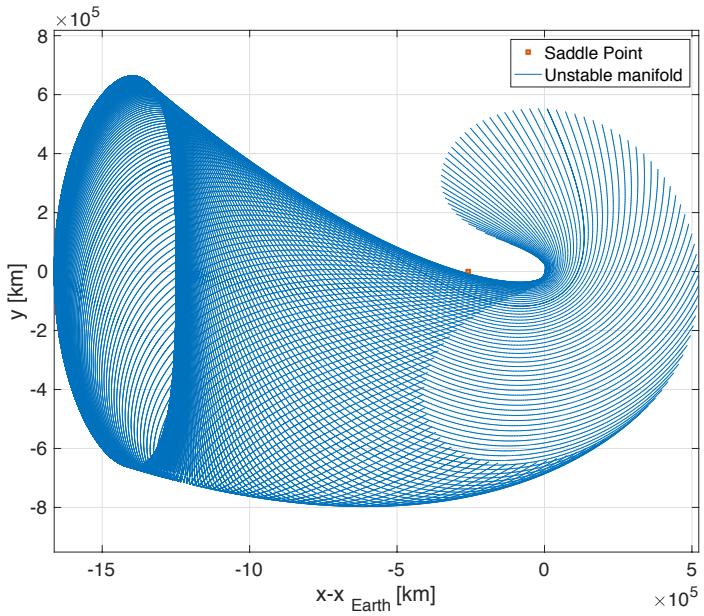

Fig. 5: Relative geometry between an L_1 halo orbit ($A_z = 10^5$ km) and the SP.

from its three-body approximation (see Table 3). As a result, for the L_1/L_2 case, 1591/903 solutions are obtained for the first SP passage, 51/54 solutions for the second SP passage, 2/8 solutions for the third SP passage, and 0/3 solutions for the fourth SP passage. The remaining cases do not feature SP distances that are less than 10,000 km within the propagation time. Relevant output for later analysis are listed in Table 6.

During the transfer, the S/C may approach the SP multiple times. This is evident in the sample transfer shown in Figure 6. The opposite of SP distance is plotted in Figure 6b. When the peak distance between the manifold and the SP becomes less than 10,000 km, a SP passage occurs with a known minimum distance. For instance, trajectory in Figure 6a has two SP passages. Ultimately, many trajectories experience close lunar encounters, defined within the lunar sphere of influence. Close lunar encounters are also referred to as lunar gravity assists (LGAs).

The scatter plot matrix is used to compactly present results. With this tool, the relationships between multiple variables can be assessed synthetically and simul-

Table 5: Bounds of the search space in the RFBP.

Symbol	Description	Unit	Range	Step
A_z	Size of the halo orbit	km	50,000 - 500,000	50,000
t_{po}	Time along the halo	–	0 - T_{po}	$T_{\mathrm{po}}/720$
α	Moon phase	degrees	0 - 360	30

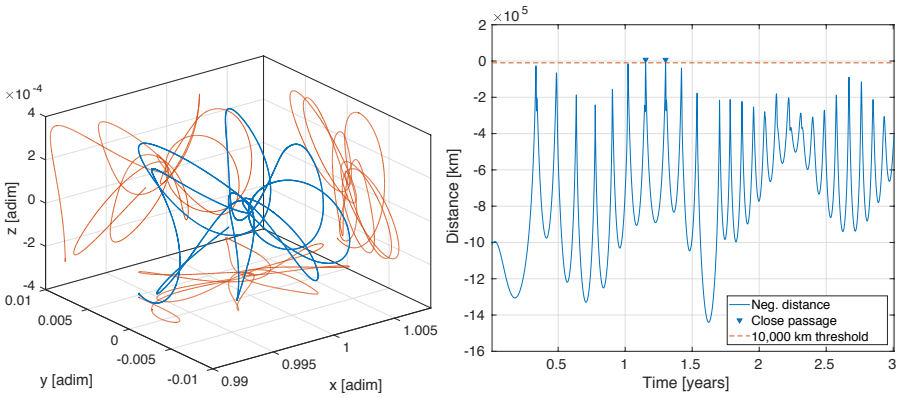

(a) Trajectory sample to SP from the halo orbit.

(b) SP distance against ToF.

Fig. 6: Sample of SP transfer.

Table 6: Output variables.

Notation	Description	Unit
$r_{\mathrm{SP}}^{\mathrm{min}}$	Distance of saddle point passage	km
t_{SP}	Time at the SP passage	years
# LGA	Number of LGA	-
$r_{\mathrm{LGA}}^{\mathrm{min}}$	Minimum distance for LGA	km
t_{LGA}	Time at the minimum distance for LGA	years

taneously. Let $\{v\}_{i,j=1}^{n}$ be a collection of n generic variables spanned by either index $i = 1, \ldots, n$ or $j = 1, \ldots, n$. The saddle point passage solutions depend on variables v. Then, the scatter plot matrix is a $n \times n$ matrix whose element in row i and column j is the standard scatter plot of the saddle point passage solutions with respect to variables v_i (along the y axis) and v_j (along the x axis). Due to the symmetric nature of the scatter plot matrix, only the lower (or upper) triangular part is relevant as it provides independent information. The i-th diagonal element of the matrix displays the histograms outlines of the SP passage solutions only as function of variable v_i. The histograms are normalized along the vertical axis such that the area of each bin is the relative number of solutions, and the sum of the bin areas is less than or equal to 1. The number and width of the bins are determined by application of Scott's rule [19].

In this work, 8 variables are used to produce the scatter plot matrix, i. e., 3 inputs and 5 outputs of the simulation. The variables are thus the minimum distance of the S/C to the saddle point and its time-stamp, the number of close lunar encounters, the minimum LGA range and its time-stamp, the originating halo out-of-plane altitude, the phase parameter, and the time along the halo. The variables units and ranges are those in Tables 5–6 for the RFBP and Tables 8–6 for the RPRnBP. Solutions are grouped into categories according to the number of saddle point passages experienced, in shapes of copper shading gradient, a lighter dot

is associated to more SP passages. To ease readability of the scatter plots, dots represent solutions with 1 saddle point passage, circles with 2, stars with 3, and crosses with 4 SP passages.

Figures 7–8 are the scatter matrix plots for the RFBP exploration from $L_{1,2}$. With reference to these two figures, the following can be said:

i. There are many solutions with short time-to-SP. The multiple SP passage generally occurs for TOF greater than one year; see plots of t_{SP} vs other parameters and histograms in position (2,2).

ii. Multiple lunar close passages provide no apparent benefits on neither saddle point fly-through distance nor time. In fact, the number of solutions drastically diminishes for increasing number of LGAs; see plots of #LGA vs other parameters and histograms in position (3,3).

iii. SP passage solutions are spread all over lunar encounter altitude domain; see plots of $r_{\mathrm{LGA}}^{\mathrm{min}}$ vs other parameters and histograms in position (4,4).

iv. Comparatively, the SP is reached more often when departing from smaller halos. Also, there are less multiple SP passage for increasing out-of-plane amplitude; see plots of A_z vs other parameters and histograms in position (6,6).

v. Moon phase loosely influences solutions, indicating successful opportunities might be gained for the n-body problem phasing; see plots of α vs other parameters and histograms in position (7,7).

vi. The multiple SP passage does not seem to have a correlation with the Moon phase and the time on the halo; see α vs t_{po} plots .

vii. Departure location has major influence. Most SP passages appear halfway along the halo ($t_{\mathrm{po}} \approx 1.6$) or tend to accumulate toward the end ($t_{\mathrm{po}} \approx 3.1$); see plots of t_{po} vs other parameters and histograms in position (8,8)

Additional direct numerical simulations are performed for non-ballistic cases. A small tangential impulsive maneuver is applied three months after the halo departure point. Although this procedure is not automated, it allows gathering insights into the sensitivity with respect to the design parameters of the SP passage distance and time. Two different impulses are considered: 0.25 m/s and 0.50 m/s. The possibility to maneuver impacts the SP passage dynamics in a twofold fashion: for increasing Δv,

1. The number of SP passages increases/decreases for the L_1/L_2 cases. A case occurs with six SP passages for $\Delta v = 0.25$ m/s departing from L_1.

2. The altitude of close SP passages generally decreases for both L_1 and L_2 cases.

The saddle point miss distance, and hence the number of SP passages, depends on the magnitude of the maneuver. The main takeaway is that even a small impulsive maneuver can significantly improve the SP miss distance. This motivates the use of explored solutions as initial guesses for a more refined optimization in which control authority is used to accurately target the SP. Thus, appropriate size and timing of the maneuvers might be used to increase the number and accuracy of SP fly-through. Table 7 shows the number of SP passages, for different maneuvers.

Table 7: Number of SP passages for ballistic and controlled cases.

Location	Δv [m/s]	Single SP passage	Multiple SP passages
L_1	0.00	1591	53
	0.25	1489	58
	0.50	1491	55
L_2	0.00	903	65
	0.25	895	55
	0.50	838	35

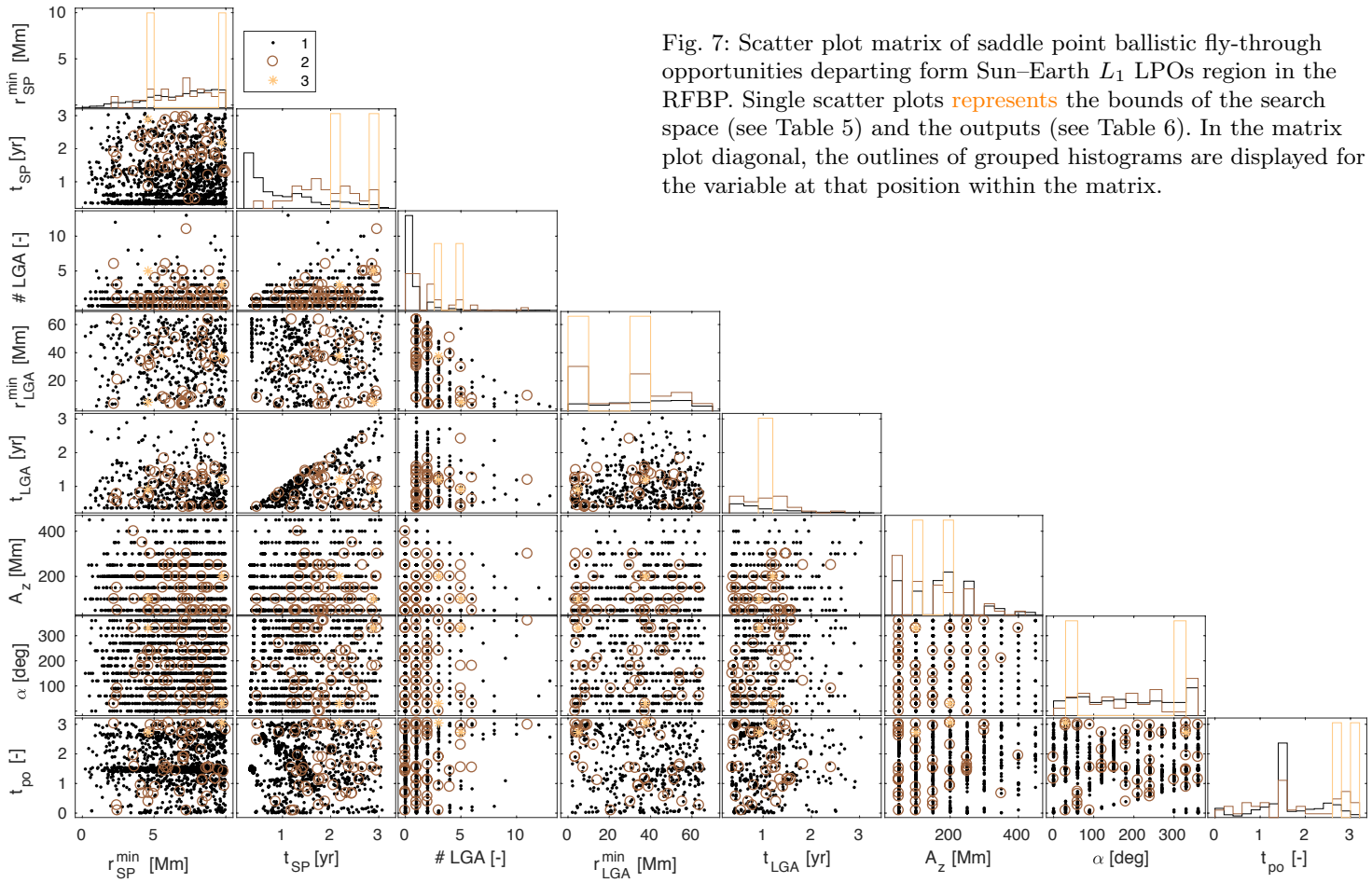

Fig. 7: Scatter plot matrix of saddle point ballistic fly-through opportunities departing form Sun–Earth L_1 LPOs region in the RFBP. Single scatter plots represents the bounds of the search space (see Table 5) and the outputs (see Table 6). In the matrix plot diagonal, the outlines of grouped histograms are displayed for the variable at that position within the matrix.

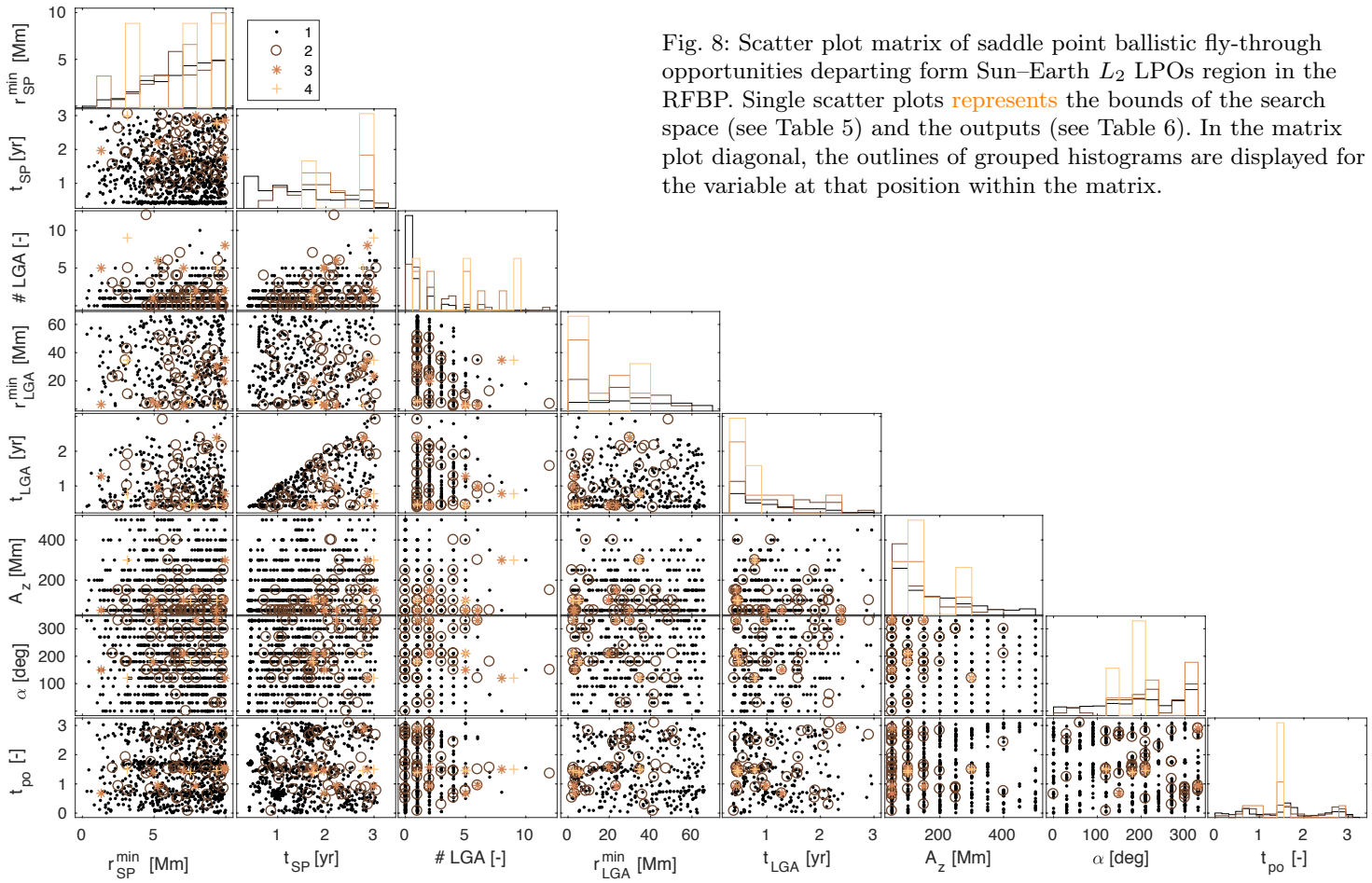

Fig. 8: Scatter plot matrix of saddle point ballistic fly-through opportunities departing form Sun–Earth L_2 LPOs region in the RFBP. Single scatter plots represents the bounds of the search space (see Table 5) and the outputs (see Table 6). In the matrix plot diagonal, the outlines of grouped histograms are displayed for the variable at that position within the matrix.

4.4 Exploration in the RPRnBP

States on the halo unstable manifolds, as defined in the CRTBP, are propagated within the RPRnBP. The nature of the problem requires specifying an initial epoch, t_0, rather than a phase angle for the Moon. The initial epoch is needed to determine the states of all celestial bodies in the model. A total of 96,000 transfers (10 A_z samples $\times$ 320 t_{po} samples $\times$ 30 t_0 samples) are computed to investigate the geometric relation between the manifold and the saddle point. Table 8 provides the bounds and resolution of the search space for the exploration in the RPRnBP. The initial epoch spans a duration of one month. This allows for a complete lunar revolution around the Earth. At this stage, the SP is assumed to follow its real trajectory, according to n-body calculation in Section 3.

Table 8: Bounds of the search space in the RPRnBP.

Symbol	Description	Units	Range	Step
A_z	Size of the halo orbit	km	50,000 - 500,000	50,000
t_{po}	Time along the halo	years	0 - T_{po}	$T_{\text{po}}/320$
t_0	Initial epoch	TDB	30 Mar 2017 - 28 Apr 2017	1 day

Figures 9–10 represent the scatter matrix plots for the RPRnBP exploration from L_1 and L_2, respectively. With reference to these two figures, the following can be said:

i. There are still many solutions with short time of flight to the saddle point. Multiple SP passages require larger TOF; see plots of t_{SP} vs other parameters and histograms in position (2,2).

ii. Many LGAs provide unfavorable conditions for repeated and close SP fly-throughs. Generally, a small number of LGA provides sufficient diversity to reach the SP ballistically; see plots of #LGA vs other parameters and histograms in position (3,3).

iii. Solutions are spread over LGA altitude domain, with a tendency for multiple SP fly-though to gather for low lunar encounter; see plots of $r_{\text{LGA}}^{\text{min}}$ vs other parameters and histograms in position (4,4).

iv. Small-halos-departing transfers offer more chances to hit the SP; see plots of A_z vs other parameters and histograms in position (6,6).

v. Initial epoch greatly influences the SP passage ballistic dynamics. In fact, no solutions exist for certain lunar configurations. These SP geometrical *holes* occur when the Moon is in opposition to the departing LPO, i. e., when the lunar perturbation is the smallest; see plots of t_0 vs other parameters and histograms in position (7,7). A magnification of the $r_{\text{SP}}^{\text{min}}$ vs t_0 plots is given in Figure 11: it provides a detailed view of the saddle point geometrical hole phenomenon for $L_{1,2}$-departing ballistic trajectories.

vi. Halo departure phasing has minor influence on SP passages dynamics, but patterns exist for proper combinations; see t_{po} vs t_0 plots.

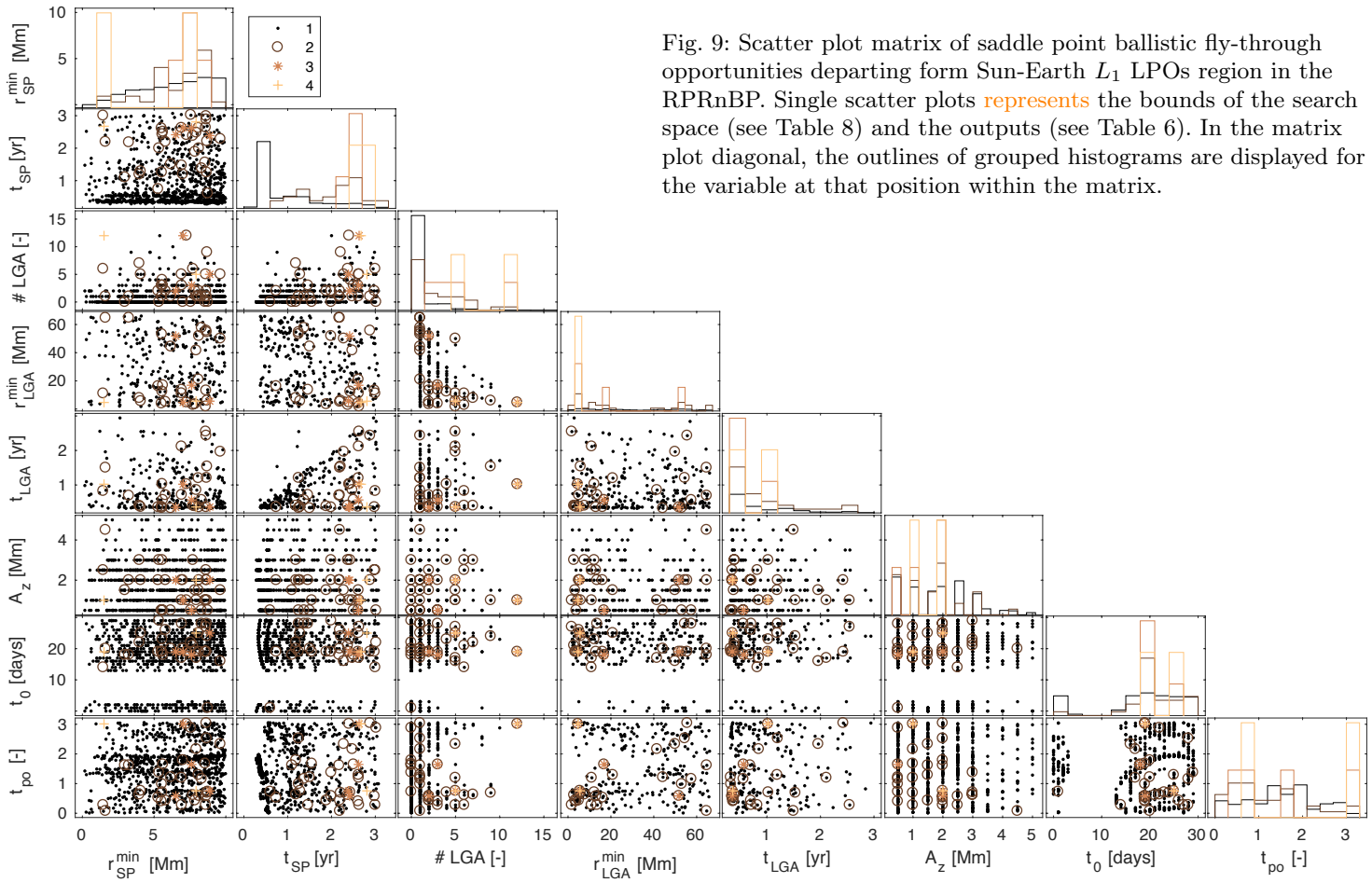

Fig. 9: Scatter plot matrix of saddle point ballistic fly-through opportunities departing form Sun-Earth L_1 LPOs region in the RPRnBP. Single scatter plots represents the bounds of the search space (see Table 8) and the outputs (see Table 6). In the matrix plot diagonal, the outlines of grouped histograms are displayed for the variable at that position within the matrix.

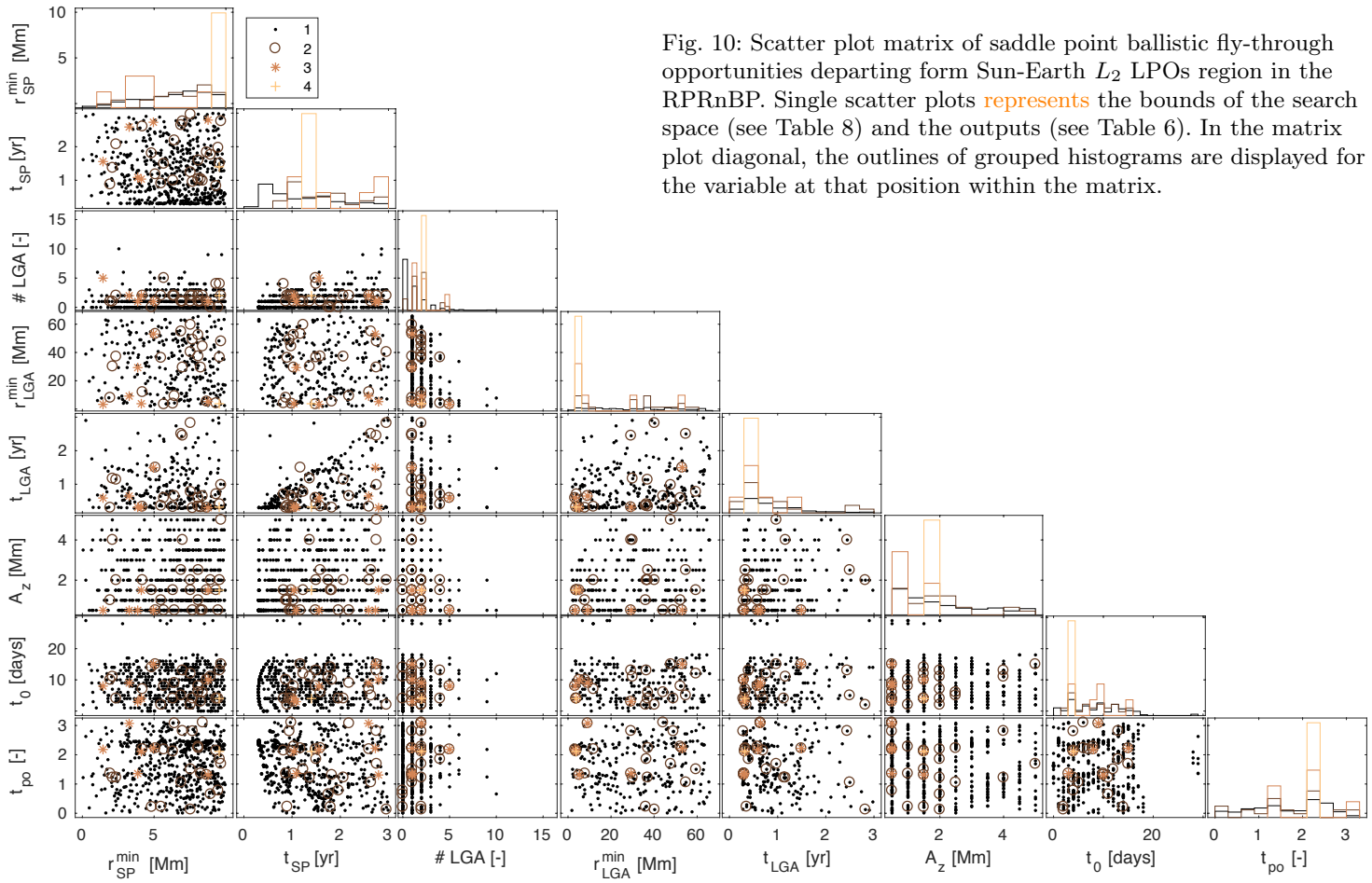

Fig. 10: Scatter plot matrix of saddle point ballistic fly-through opportunities departing form Sun-Earth L_2 LPOs region in the RPRnBP. Single scatter plots represents the bounds of the search space (see Table 8) and the outputs (see Table 6). In the matrix plot diagonal, the outlines of grouped histograms are displayed for the variable at that position within the matrix.

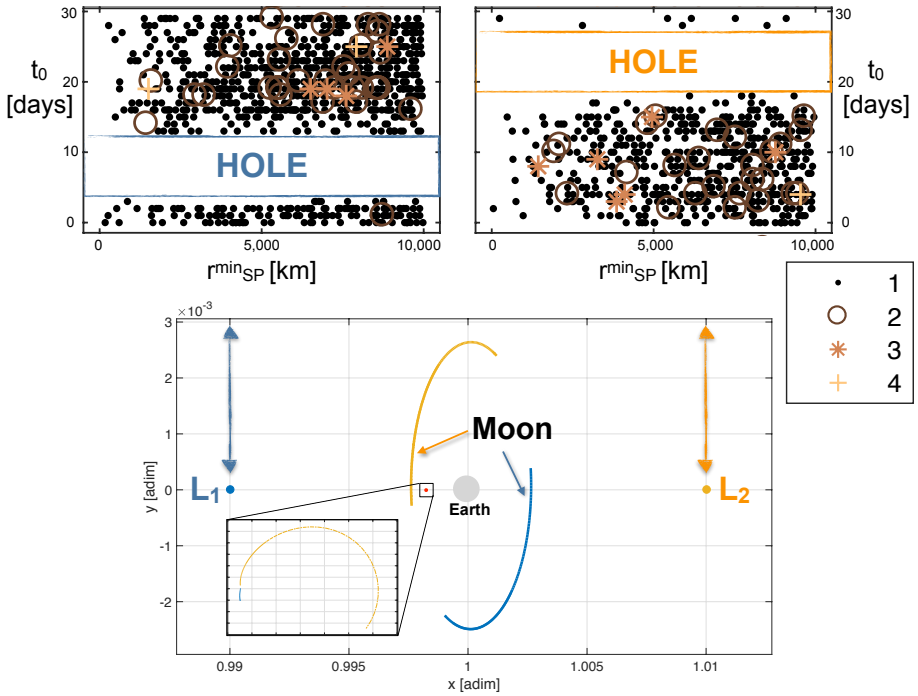

Fig. 11: Saddle point geometrical hole for the L_1 (top left) and L_2 (top right) cases, and the corresponding Moon and SP trajectories (bottom). The SP trajectory is encased.

4.5 Exploration summary

Table 9 summarizes the exploration direct numerical simulation discriminating for different dynamical models. Specifically, the values reported in Table 9 are the percentile numbers of solutions that experience one or more saddle point passages. The normalization is done with respect to the total number of initial conditions in the corresponding model. Notably,

1. No multiple SP passage solutions exist within the CRTBP;

2. The influence of a planar Moon in the bicircular RFBP is beneficial for the number of saddle points fly-through and for multiple SP passages;

3. The contribution of several gravitational attractors and perturbations in the high-fidelity model slightly penalizes SP transfers performances, yet providing sufficient diversity in the search space to motivate an optimization campaign.

Table 9: Indicator of SP passages in different dynamical models.

%	SP passage	CRTBP	RFBP	RPRnBP
L_1	Single	1.650	1.841	0.981
	Multiple	0.000	0.061	0.034
L_2	Single	0.500	1.045	0.602
	Multiple	0.000	0.075	0.026

5 Conclusion

The Sun–Earth gravitational saddle point geometrical and dynamical properties have been characterized. The saddle point trajectory is analyzed in the CRTBP, RFBP, and RPRnBPP. Evidence is given that flying through a 10,000 km bubble around the saddle point can be achieved in a ballistic fashion from the Sun–Earth $L_{1,2}$ libration point orbits region. The highly nonlinear and nonequilibrium nature of the vector field in the vicinity of the saddle point are exploited to find many orbits ballistically approaching the Sun–Earth SP. In turn, this suggests that a limited-resources spacecraft may feasibly and accurately fly through the saddle point. With the proper payload, measurements of background acceleration gradients can be taken to test and assess the validity of alternative gravitational theories.

Trajectories that fly through the saddle point neighborhood one or multiple times are more numerous when departing from the Sun–Earth L_1 libration point orbit region. An opportunistic mission would thus achieve better results if departing from L_1. However, the difference in performances between L_1 and L_2 LPOs is not so marked to exclude mission extension scenarios for spacecraft orbiting at Sun–Earth L_2.

Acknowledgements Part of the work described in this paper has been conducted under ESA Contract No. 4000118201/16/F/MOS. The authors would like to acknowledge Florian Renk, Gonçalo Aguiar, Erind Veruari, Srikara Cherukuri, and Carmine Giordano for their valuable contributions.

Conflict of Interest: The authors declare that they have no conflict of interest.

References

1. Acton Jr, C.: Ancillary data services of nasa's navigation and ancillary information facility. Planetary and Space Science **44**(1), 65–70 (1996). DOI 10.1016/0032-0633(95)00107-7
2. Acton Jr, C., Bachman, N., Semenov, B., Wright, E.: A look towards the future in the handling of space science mission geometry. Planetary and Space Science **150**, 9–12 (2018). DOI 10.1016/j.pss.2017.02.013
3. Bekenstein, J., Magueijo, J.: Modified Newtonian dynamics habitats within the solar system. Physical Review D **73**, 103,513.1–14 (2006). DOI 10.1103/PhysRevD.73.103513
4. Belbruno, E., Miller, J.: Sun-perturbed Earth-to-Moon transfers with ballistic capture. Journal of Guidance, Control, and Dynamics **16**(4), 770–775 (1993). DOI 10.2514/3.21079

5. Cox, A., Howell, K.: Transfers to a Sun–Earth Saddle Point: An Extended Mission Design Option for LISA Pathfinder. Advances in the Astronautical Sciences **158**(I), 653–668 (2016)
6. Dei Tos, D., Topputo, F.: On the advantages of exploiting the hierarchical structure of astrodynamical models. Acta Astronautica **136**, 236–247 (2017). DOI 10.1016/j.actaastro.2017.02.025
7. Dei Tos, D., Topputo, F.: Trajectory refinement of three-body orbits in the real solar system model. Advances in Space Research **59**(8), 2117–2132 (2017). DOI 10.1016/j.asr.2017.01.039
8. Fabacher, E., Kemble, S., Trenkel, C., Dunbar, N.: Multiple Sun–Earth saddle point flybys for LISA Pathfinder. Advances in Space Research **52**(1), 105–116 (2013). DOI 10.1016/j.asr.2013.02.005
9. Galianni, P., Feix, M., Zhao, H.S., Horne, K.: Testing quasilinear modified Newtonian dynamics in the solar system. Physical Review D **86**, 044,002 1–18 (2012). DOI 10.1103/PhysRevD.86.044002
10. Gómez, G., Masdemont, J., Mondelo, J.: Solar system models with a selected set of frequencies. Astronomy and Astrophysics **390**(2), 733–750 (2002). DOI 10.1051/0004-6361:20020625
11. Howell, K.: Three-dimensional, periodic, 'halo' orbits. Celestial mechanics **32**(1), 53–71 (1984). DOI 10.1007/BF01358403
12. Howell, K., Pernicka, H.: Numerical determination of lissajous trajectories in the restricted three-body problem. Celestial Mechanics and Dynamical Astronomy **41**(1), 107–124 (1987). DOI 10.1007/BF01238756
13. Jehn, R., Campagnola, S., Garcia, D., Kemble, S.: Low-thrust approach and gravitational capture at Mercury. In: 18th International Symposium on Space Flight Dynamics, vol. 548, pp. 487–492 (2004)
14. Luo, Z., Topputo, F., Bernelli-Zazzera, F., Tang, G.: Constructing ballistic capture orbits in the real solar system model. Celestial Mechanics and Dynamical Astronomy **120**(4), 433–450 (2014). DOI 10.1007/s10569-014-9580-5
15. Marquardt, D.: An algorithm for least-squares estimation of nonlinear parameters. Journal of the society for Industrial and Applied Mathematics **11**(2), 431–441 (1963). DOI 10.1137/0111030
16. Milgrom, M.: A modification of the Newtonian dynamics as a possible alternative to the hidden mass hypothesis. Astrophysical Journal **270**, 365–370 (1983). DOI 10.1086/161130
17. Milgrom, M.: The MOND paradigm. arXiv preprint astro-ph/0801.3133 (2008)
18. Milgrom, M.: Testing the MOND paradigm of modified dynamics with galaxy-galaxy gravitational lensing. Physical Review Letters **111**, 041,105 1–5 (2013). DOI 10.1103/PhysRevLett.111.041105
19. Scott, D.: Scott's rule. Wiley Interdisciplinary Reviews: Computational Statistics **2**(4), 497–502 (2010). DOI 10.1002/wics.103
20. Szebehely, V.: Theory of orbits: the restricted problem of three bodies. Academic Press, New York (1967)
21. Topputo, F.: On optimal two-impulse Earth–Moon transfers in a four-body model. Celestial Mechanics and Dynamical Astronomy **117**(3), 279–313 (2013). DOI 10.1007/s10569-013-9513-8
22. Topputo, F.: Fast numerical approximation of invariant manifolds in the circular restricted three-body problem. Communications in Nonlinear Science and Numerical Simulation **32**(Supplement C), 89–98 (2016). DOI 10.1016/j.cnsns.2015.08.004
23. Topputo, F., Belbruno, E.: Earth–Mars transfers with ballistic capture. Celestial Mechanics and Dynamical Astronomy **121**(4), 329–346 (2015). DOI 10.1007/s10569-015-9605-8
24. Topputo, F., Dei Tos, D., Rasotto, M., Renk, F.: Design and validation of ultra low thrust transfers to the Sun–Earth saddle point with application to LISA Pathfinder mission extension. In: 26th International Symposium on Space Flight Dynamics, 3–9 June 2017, Matsuyama, Japan (2017)
25. Topputo, F., Dei Tos, D., Rasotto, M., Renk, F.: Design and feasibility assessment of ultra low thrust trajectories to the Sun–Earth saddle point. In: 28th AIAA/AAS Space Flight Mechanics Meeting, Kissimmee, Florida, USA (2018)
26. Trenkel, C., Kemble, S.: Gravitational science with LISA Pathfinder. Journal of Physics: Conference Series **154**(1), 012,002 (2009). DOI 10.1088/1742-6596/154/1/012002
27. Trenkel, C., Kemble, S., Bevis, N., Magueijo, J.: Testing modified Newtonian dynamics with LISA Pathfinder. Advances in Space Research **50**(11), 1570–1580 (2012). DOI 10.1016/j.asr.2012.07.024

28. Trenkel, C., Wealthy, D.: Effect of LISA Pathfinder spacecraft self-gravity on anomalous gravitational signals near the Sun–Earth saddle point predicted by quasilinear mond. Physical Review D **90**, 084,037.1–22 (2014). DOI 10.1103/PhysRevD.90.084037